

# The mass of the black hole in Centaurus A from SINFONI AO-assisted integral-field observations of stellar kinematics

Michele Cappellari,<sup>1\*</sup> N. Neumayer,<sup>2</sup> J. Reunanen,<sup>3</sup> P. P. van der Werf,<sup>4</sup>  
P. T. de Zeeuw<sup>2,4</sup> and H.-W. Rix<sup>5</sup>

<sup>1</sup> *Sub-Department of Astrophysics, University of Oxford, Denys Wilkinson Building, Keble Road, Oxford OX1 3RH*

<sup>2</sup> *European Southern Observatory, Karl-Schwarzschild-Str 2, 85748 Garching, Germany*

<sup>3</sup> *Tuorla Observatory, University of Turku, Väisäläntie 20, 21500 Piikkiö, Finland*

<sup>4</sup> *Leiden Observatory, Leiden University, P.O. Box 9513, 2300 RA Leiden, The Netherlands*

<sup>5</sup> *Max-Planck Institute for Astronomy, Königstuhl 17, 69117 Heidelberg, Germany*

Accepted for publication in MNRAS

## ABSTRACT

We present a determination of the mass of the supermassive black hole (BH) and the nuclear stellar orbital distribution of the elliptical galaxy Centaurus A (NGC 5128) using high-resolution integral-field observations of the stellar kinematics. The observations were obtained with SINFONI at the ESO Very Large Telescope in the near-infrared ( $K$ -band), using adaptive optics to correct for the blurring effect of the earth atmosphere. The data have a spatial resolution of  $0''.17$  FWHM and high  $S/N \gtrsim 80$  per spectral pixel so that the shape of the stellar line-of-sight velocity-distribution can be reliably extracted. We detect clear low-level stellar rotation, which is counter-rotating with respect to the gas. We fit axisymmetric three-integral dynamical models to the data to determine the best fitting values for the BH mass  $M_{\text{BH}} = (5.5 \pm 3.0) \times 10^7 M_{\odot}$  ( $3\sigma$  errors) and  $(M/L)_K = (0.65 \pm 0.15)$  in solar units. These values are in excellent agreement with previous determinations from the gas kinematics, and in particular with our own published values, extracted from the same data. This provides one of the cleanest gas versus stars comparisons of  $M_{\text{BH}}$  determination, due to the use of integral-field data for both dynamical tracers and due to a very well resolved BH sphere of influence  $R_{\text{BH}} \approx 0''.70$ . We derive an accurate profile of the orbital anisotropy and we carefully test its reliability using spherical Jeans models with radially varying anisotropy. We find an increase in the tangential anisotropy close to the BH, but the spatial extent of this effect seems restricted to the size of  $R_{\text{BH}}$  instead of that  $R_b \approx 3''.9$  of the core in the surface brightness profile, contrary to detailed predictions of current simulations of the binary BH scouring mechanism. More realistic simulations would be required to draw conclusions from this observation.

**Key words:** black hole physics – galaxies: individual (NGC 5128) – galaxies: elliptical and lenticular, cD – galaxies: kinematics and dynamics – instrumentation: adaptive optics

## 1 INTRODUCTION

The existence of supermassive black holes (BHs) in normal galaxy nuclei was predicted forty years ago by Lynden-Bell (1969), but until fifteen years ago it was still considered an interesting possibility which had to be demonstrated. Nowadays BHs are regarded as a crucial ingredient for our understanding of how galaxies form. Key to this paradigm shift was the launch in 1990 of the Hubble Space Telescope (HST). It all started with the realisation that the mass of the BH is correlated to other global characteristics of the host galaxy as a whole. Initially a correlation  $M_{\text{BH}} - L$  was found between the mass of the BH and the luminosity of the host-galaxy stellar spheroid (Kormendy & Richstone 1995; Magorrian et al. 1998).

In 1997 the installation of the STIS long-slit spectrograph on HST allowed the spatially-resolved kinematical observations to probe inside the radius of the subarcsecond BH sphere of influence  $R_{\text{BH}} \equiv GM_{\text{BH}}/\sigma^2$  in nearby galaxies ( $\sigma$  being the velocity dispersion of the stars in the galaxy). The increased accuracy in the  $M_{\text{BH}}$  determinations contributed to the discovery of the tighter  $M_{\text{BH}} - \sigma$  correlation (Ferrarese & Merritt 2000; Gebhardt et al. 2000).

As  $\sigma$  is a good predictor of galaxy properties, it is perhaps not surprising that similar correlations were found between  $M_{\text{BH}}$  and respectively the galaxy concentration (Graham et al. 2001), the dark-halo mass (Ferrarese 2002; Baes et al. 2003; Pizzella et al. 2005), the bulge mass (McLure & Dunlop 2002; Marconi & Hunt 2003; Häring & Rix 2004) and the stars' gravitational binding energy (Aller & Richstone 2007). The existence of these correlations is broadly consistent with a scenario in which the BH regulates

\* E-mail: cappellari@astro.ox.ac.uk

the galaxy formation, during the hierarchical galaxy merging, by shutting off the conversion of gas into stars via a feedback mechanism due to its powerful outflows (Silk & Rees 1998; Granato et al. 2004; Di Matteo et al. 2005; Bower et al. 2006).

Even though the current scenario explains a number of observed facts, our interpretation of the role of BHs in galaxy formation is far from secure. One of the problems lies in the fact that the models have few observables to compare with, mainly the galaxy mass (or  $\sigma$ ) and  $M_{\text{BH}}$ . Moreover, even after a decade of HST spectroscopy and models, only about 40 secure BH determinations exist (compilations are given e.g. in Tremaine et al. 2002; Ferrarese & Ford 2005; Graham 2008). With few exceptions the BH determinations have been performed with a single dynamical tracer (either gas or stars), so that no independent test of the two measurements methods could be made. Very little is known about the orbital distribution near the BHs, which is expected to contain key information on the BH accretion process (Quinlan & Hernquist 1997; Milosavljević & Merritt 2001).

The advent of integral-field spectroscopy on all the 8–10-m class telescopes, combined with adaptive optics (AO) to reduce the blurring effect of the Earth’s atmosphere is opening a new epoch for BH studies. The large mirrors allow for shorter exposure times and higher signal-to-noise ratios ( $S/N$ ) of the observations, than what was possible with the 2.4-m mirror and the STIS long-slit spectrograph of HST. Observations at near-infrared wavelengths allow dust absorption effects to be virtually eliminated. The integral-field observations, due to the tight constraint on the orbital distribution, dramatically improve the accuracy of  $M_{\text{BH}}$  determination, for a given spatial resolution and  $S/N$  (Verolme et al. 2002). Integral-field data are also needed for a unique recovery of the orbital distribution from the observations (Cappellari & McDermid 2005; Krajnović et al. 2005; van de Ven et al. 2008). This can be understood from dimensional arguments, considering that most orbits in a stationary potential conserve three isolating integrals of motion. This three-dimensional orbital distribution cannot be recovered without the knowledge of at least another three-dimensional observed quantity. Motivated by these arguments,  $M_{\text{BH}}$  determinations from AO-assisted integral-field observations in the near-infrared are starting to appear in the literature (Davies et al. 2006; Nowak et al. 2007, 2008).

The elliptical galaxy NGC 5128 (Centaurus A) is a prime candidate for AO-assisted integral-field observations. At least nine independent distance  $D$  determinations for Cen A, based on different methods, are available in the literature<sup>1</sup> (e.g. Tonry et al. 2001; Rejkuba 2004; Ferrarese et al. 2007). The median value is  $D = 3.8$  Mpc, with extreme ranges of 3.4 Mpc and 4.4 Mpc respectively. Here we adopt a value<sup>2</sup>  $D = 3.5$  Mpc to be consistent with all the earlier papers on  $M_{\text{BH}}$  determination on this galaxy (Marconi et al. 2001, 2006; Silge et al. 2005; Häring-Neumayer et al. 2006; Krajnović et al. 2007; Neumayer et al. 2007). At this close distance Cen A is the nearest elliptical galaxy and one arcsec corresponds to 17 pc.

Cen A is among the only  $\sim 10$  galaxies on the whole sky with an observed  $R_{\text{BH}} \approx 1''$  (see Kormendy 2004, for a partial list). Moreover Cen A possesses a nuclear gaseous disk in regular rotation from which a number of independent determinations of  $M_{\text{BH}}$

have been performed, with ever increasing accuracy (Marconi et al. 2001, 2006; Häring-Neumayer et al. 2006; Krajnović et al. 2007; Neumayer et al. 2007). This allows for an accurate comparison between the BH mass derived with gaseous or stellar kinematics. The  $K$ -band central surface brightness of Cen A is quite bright at  $\mu_K \approx 12.2$  mag (Jarrett et al. 2003), which allows a high  $S/N$  in the stellar spectra to be achieved in reasonable exposure times. A bright star, sufficiently close to the nucleus, can be used as reference for the AO correction. All these facts make Cen A a unique observational benchmark for  $M_{\text{BH}}$  determinations in the near-infrared.

In Section 2 we describe our data and the extraction of the stellar kinematics. In Section 3 we present the stellar dynamical models. We discuss our results in Section 4 and we finally summarize them in Section 5.

## 2 OBSERVATIONS AND DATA ANALYSIS

### 2.1 Spectroscopic data

For the dynamical modeling of the stellar kinematics we used integral-field spectroscopy obtained with SINFONI on the UT4 (Yepun) of the Very Large Telescope of the European Southern Observatory on the Cerro Paranal. SINFONI consists of the cryogenic near-IR integral field spectrometer SPIFFI (Eisenhauer et al. 2003a,b) coupled to the visible curvature AO system MACAO (Bonnet et al. 2003). We observed the nucleus of Cen A with two different spatial scales:  $0''.250 \times 0''.125$  (250mas scale) with a Field of View (FoV) of  $8'' \times 8''$  and  $0''.10 \times 0''.05$  (100mas scale) with a FoV of  $3''.2 \times 3''.2$ . The 100mas observations and data reduction were already described in Neumayer et al. (2007). The observations were performed in excellent seeing conditions of  $0''.5$  FWHM, as measured by the seeing monitor in the  $V$ -band. With the 250mas spatial scale the observations were taken in natural seeing, while with the 100mas scale the SINFONI AO module was locked onto an  $R \sim 14$  mag star about  $36''$  southwest of the nucleus. Although the reference star is relatively distant from the galaxy nucleus, the good seeing allowed us to achieve a nearly diffraction-limited correction in the  $K$ -band. Both data sets were obtained in the  $K$ -band, which covers the wavelength range  $1.93\text{--}2.47\mu\text{m}$ . The spectral resolution of the observations was  $R \sim 4800$  in both scales, and corresponds to an instrumental dispersion of  $\sigma_{\text{ins}} \sim 27 \text{ km s}^{-1}$ .

The 250mas observations followed an Object-Sky-Object sequence with equal exposure time of 300 s each, for a total on-source exposure time of  $4 \times 300 = 1,200$  s. The sky exposure were taken at  $200''$  from the nucleus to make sure the spectra were not contaminated by the large galaxy. The 100mas observations followed a similar sequence with individual exposure times of 900 s each and a total on-source exposure time of  $15 \times 900 = 13,500$  s. The different exposures were dithered with shifts of  $0''.2$  to allow for the removal of detector defects and cosmic rays. The data were reduced using the SINFONI data reduction pipeline provided by ESO as described in section 2 of Neumayer et al. (2007).

The spatial point-spread-function (PSF) of the 100mas observation was determined in section 2.1 of Neumayer et al. (2007) from a fit to the non-thermal nucleus, which is unresolved down to a  $0''.06$  (FWHM) spatial resolution (Häring-Neumayer et al. 2006; Marconi et al. 2006). The PSF can be approximated by two Gaussians with FWHM of  $0''.12$  and  $0''.30$  respectively, with the smallest Gaussian containing 17% of the total flux. A two-dimensional fit with a single Gaussian to the nucleus in the reconstructed image from the data cube gives a FWHM of  $0''.17$ .

<sup>1</sup> See the NED-1D compilation by Barry F. Madore and Ian P. Steer at <http://nedwww.ipac.caltech.edu/level5/NED1D/>.

<sup>2</sup> The choice of the distance  $D$  does not affect our results but sets the scale of our models in physical units. Specifically, lengths and masses scale as  $D$ , while mass-to-light ratios scale as  $D^{-1}$ .

For the stellar dynamical modeling the integral-field high-spatial resolution SINFONI observations are essential to tightly constrain the BH mass and stellar orbital distribution. However they are not sufficient as they sample only a small fraction of the half-light radius of Cen A ( $R_e \approx 83''$  in  $K$ -band; Jarrett et al. 2003). Shapiro et al. (2006) showed that one has to sample with the kinematics a significant fraction of  $R_e$  to accurately constrain BH masses. For this reason in this paper we also use the  $K$ -band kinematics obtained with the Gemini Near Infrared Spectrograph (GNIRS) at Gemini South by Silge et al. (2005). The long-slit observations extend to a distance of  $R \approx 40''$  from the galaxy nucleus and were obtained at two position angles: (i) centered on the nucleus, along the galaxy major axis at large radii ( $PA_{\text{phot}} \approx 35^\circ$  from North through East), and (ii) along the galaxy minor axis ( $PA_{\text{phot}} \approx 125^\circ$ ), but offset from the nucleus by  $0''.85$ . In this paper we increased the GNIRS  $\sigma$  by 5% to match our SINFONI kinematics. Differences at this level between the two datasets are almost unavoidable and are likely due to low-level systematic calibration errors, or differences in the adopted stellar templates. For this reason we cannot state which of the two datasets has the proper absolute  $\sigma$  calibration. As none of the results in this paper depends on whether we apply the small shift to the GNIRS or SINFONI data, we arbitrarily decided to increase the GNIRS data to match our SINFONI ones, which we adopt as reference. A 5% uncertainty in  $\sigma$  approximately translates into a 10% uncertainty in the  $M/L$ .

## 2.2 Merging and binning

The individual SINFONI exposures were registered using reconstructed images and merged into a single data cube. In the process they were resampled to a spatial scale of  $0''.125 \times 0''.125$  (250mas scale) and  $0''.05 \times 0''.05$  (100mas scale).

The stellar kinematics requires a high  $S/N$  for an unbiased extraction from the spectra. For typical observational setups, values on the order of  $S/N \gtrsim 50$  per spectral pixel, are generally required to detect deviations of the line-of-sight velocity distribution from a simple Gaussian shape (e.g. van der Marel & Franx 1993; Bender et al. 1994; Statler 1995). For this reason long-slit data are invariably adaptively binned along the spatial direction, before the kinematic extraction (e.g. van der Marel 1994). The goal of binning is to maintain the maximum spatial resolution, given a constraint on the minimum  $S/N$ . For our integral-field data we use the Voronoi binning technique,<sup>3</sup> which constitutes an optimal solution to this problem in two-dimension (Cappellari & Copin 2003).

Given that the observations are dominated by the photon noise, we spatially binned the data by requiring an equal number of counts in each spatial bin. In this way we did not have to rely on the, often inaccurate, noise propagation by the reduction pipeline, to estimate the  $S/N$ . This constant flux per bin is achieved in the Voronoi binning algorithm by setting the input noise  $N = \sqrt{S}$ , where  $S$  is the total flux (in arbitrary units) in each unbinned spectrum. For the 100mas scale the target  $S/N$  for the binning was fixed by the requirement for the data to be unbinned (pixel size  $0''.05 \times 0''.05$ ) within a radius  $R \lesssim 0''.2$  and start being binned at larger radii, where the surface brightness decreases. This led to 622 Voronoi bins, out of the original  $64^2 = 4096$  pixels. Similarly for the 250mas scale we required the data to be unbinned (pixel size  $0''.125 \times 0''.125$ ) within  $R \lesssim 0''.5$ , leading to 554 bins. The actual minimum  $S/N$  achieved by the adopted binning was determined afterwards, from

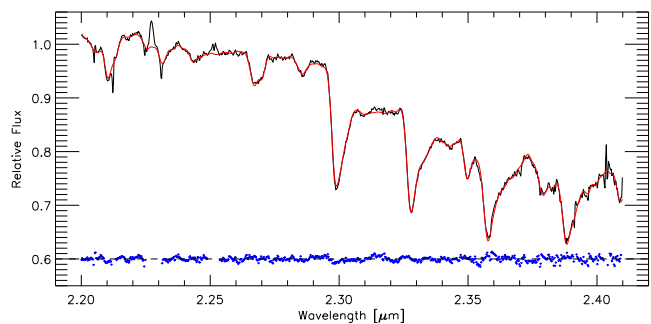


**Figure 1.** Optimal template for Cen A. The total galaxy spectrum observed with SINFONI within the  $8'' \times 8''$  250mas field (black solid line) is compared to the broadened optimal template determined with pPXF (red solid line). The fit residuals, vertically shifted by an arbitrary amount, are shown as blue dots. The gaps in the residuals correspond to some non well corrected telluric features and two  $H_2$  gas emission lines at  $2.23\mu\text{m}$  and  $2.25\mu\text{m}$ , which were excluded from the fit.

the rms residuals of a spectral template fit (Section 2.3), to be  $(S/N)_{\text{min}} \sim 80$  for both spatial scales.

## 2.3 Extraction of the stellar kinematics

The near-infrared  $K$ -band spectral region is dominated by the strong stellar absorption feature of the  $2.30\mu\text{m}$  (2-0)  $^{12}\text{CO}$  band head. At this wavelength the galaxy spectrum is dominated by the light from cool and evolved giant stars. The strength of the CO absorption is very sensitive to the star surface gravity (Kleinmann & Hall 1986; Wallace & Hinkle 1997) and this implies that, contrary to the optical region, in the  $K$ -band it is *essential* to include giant stars in the construction of an optimal stellar template for an unbiased extraction of the stellar kinematics (Silge & Gebhardt 2003).

The extraction of the stellar kinematics was performed using the penalized pixel-fitting method<sup>3</sup> (pPXF; Cappellari & Emsellem 2004), which fits the logarithmically-rebinned spectra with a template convolved with a line-of-sight velocity-distribution described by a Gauss-Hermite expansion (van der Marel & Franx 1993; Gerhard 1993). The method allows the template to be carefully optimized during the kinematics fit, it permits emission lines to be easily masked, and it includes a penalty criterion to deal with low  $S/N$  or insufficient resolution in the spectra. As library of stellar templates we used a set of 11 dwarfs and giants stars (luminosity class II–V) of late spectral types (K–M), observed with the same instrumental setup as for the Cen A observations.

The optimal positive linear combination of the 11 templates was determined only once, using a spectrum with very high  $S/N \approx 240$ , obtained by co-adding all the spectra in the 250mas SINFONI observations, while excluding the unresolved non-stellar nucleus. As expected the flux in the resulting optimal template fit is dominated by a giant M5III star (52% of the flux). This star provides by itself an excellent fit to the central spectrum of Cen A. However the contribution from a dwarf M0V star (30% of the flux) is required to properly reproduce the depth of the Na feature at  $2.21\mu\text{m}$  (cf. Lyubenova et al. 2008). The template provides a very accurate description of the spectrum from  $2.2\mu\text{m}$ – $2.4\mu\text{m}$ , which contains all the significant stellar absorption features in the  $K$ -band (Fig. 1).

For maximum consistency the same combination of stellar templates was used to extract the kinematics at all spatial positions and for both the 250mas and 100mas observations. Additive poly-

<sup>3</sup> Available from <http://www-astro.physics.ox.ac.uk/~mxc/idl/>

nomials of degree four were used to allow for possible variations in the stellar line-strength at different radii, to account for imperfections in the sky subtraction or spectral calibration, and to model the contribution of the non-thermal nucleus (Section 2.4). Consistent results were obtained using polynomials of degree 1–8. From numerous tests on other galaxies we found that, even for the most extreme gradients in the stellar population, the additive polynomials are sufficient to approximate possible low-frequency variations in the line-strength, once the global galaxy template is accurately determined from a high- $S/N$  spectrum, to account for the high-frequency content in the spectrum. We prefer this faster and more robust approach than trying to fit the template mix in every bin, from spectra of lower  $S/N$ . Generally both approaches give nearly indistinguishable results, and we tested that this is true also in the present case.

We fitted with pPXF the mean velocity  $V$ , the velocity dispersion  $\sigma$  and the first two Gauss-Hermite parameters  $h_3$  and  $h_4$  (van der Marel & Franx 1993; Gerhard 1993), using the same spectral range and masked regions as in the real data. We adopted a penalty  $\lambda = 0.6$  (defined in equation 12 of Cappellari & Emsellem 2004). The LOSVD is always very well sampled by our observations and the  $S/N$  is high, so any  $\lambda \lesssim 0.6$  gives essentially the same results and the measurements are virtually unbiased (Fig. 2). The  $1\sigma$  measurement errors were determined as the biweight dispersion (Hoaglin et al. 1983) of 100 Monte Carlo realizations. For the determination of realistic errors we used non-penalized fits with  $\lambda = 0$ . At our minimal  $S/N \approx 80$  and for  $\sigma \approx 150 \text{ km s}^{-1}$  the typical random errors in  $V$ ,  $\sigma$ ,  $h_3$  and  $h_4$ , are  $4 \text{ km s}^{-1}$ ,  $5 \text{ km s}^{-1}$ ,  $0.02$  and  $0.03$  respectively. The kinematics extraction was performed while fitting precisely the same wavelength region, from  $2.25\mu\text{m}$ – $2.37\mu\text{m}$ , in both the 250mas and 100mas SINFONI observations (Fig. 5). This spectral region includes the (2–0)  $^{12}\text{CO}$  band head and three other prominent band heads of the  $^{12}\text{CO}$  series. Emission from the highly ionized species of [CaVIII] at  $2.32\mu\text{m}$  and an  $\text{H}_2$  line at  $2.35\mu\text{m}$  were excluded from the fits (see also Riffel et al. 2008).

The extracted SINFONI kinematics<sup>4</sup> in the two scales is shown in Fig. 3 and Fig. 4. For the first time our observations detect a low-level clear sense of stellar rotation in Cen A. We used the method of Appendix C of Krajnović et al. (2006) to determine the global kinematical major axis  $\text{PA}_{\text{kin}} = 167^\circ \pm 8^\circ$  and the systemic velocity of  $V_{\text{sys}} = 531 \pm 5 \text{ km s}^{-1}$ . A maximum velocity of just  $\Delta V \approx 20 \text{ km s}^{-1}$  is reached along  $\text{PA}_{\text{kin}}$  at about  $R \approx 4''$  from the nucleus, at the edge of our 250mas SINFONI FoV. The  $\sigma$  field shows a gradual increase towards the center, before a sudden drop in the very center, where the non-thermal continuum prevents a proper kinematics extraction. The  $h_3$  field is symmetric about the center, indicating low template-mismatch, and anti-correlated with  $V$ , as generally observed in early-type galaxies (Bender et al. 1994; Krajnović et al. 2008), and the  $h_4$  field is generally close to zero over the whole field.

The nuclear stellar rotation is *counter-rotating* (by about  $180^\circ$ ) with respect to the regular  $\text{H}_2$  nuclear gas rotation presented in Neumayer et al. (2007, their fig. 6). The stars also rotate much slower than the gas, which reaches a maximum velocity  $\Delta V \approx 130 \text{ km s}^{-1}$  at  $R \approx 0''.5$ . This indicates that the recent gas acquisition was not able to produce a significant fraction of stars near the nucleus. This is consistent with the lack of evidence for any change in the nuclear stellar population of Cen A. This is different from a sim-

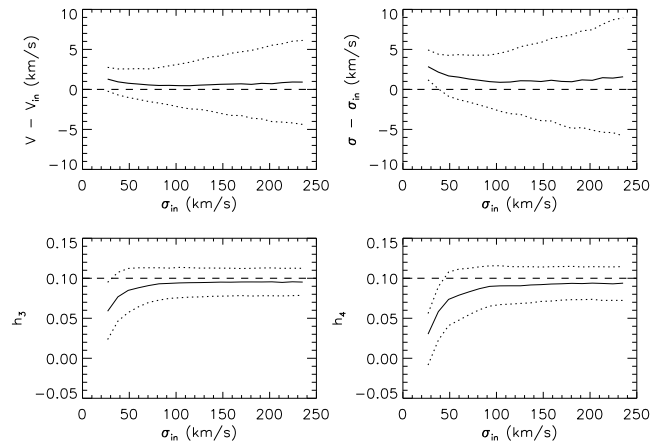


**Figure 2.** Testing of penalization in pPXF. We simulated spectra with the  $S/N = 80$  of our data and an LOSVD with  $h_3 = 0.1$ ,  $h_4 = 0.1$  and  $\sigma$  in the range between 30 and  $240 \text{ km s}^{-1}$ . We extracted the kinematics with pPXF and a penalty  $\lambda = 0.6$ . The lines in the top two panels show the 50th (median, solid line), 16th and 84th percentiles ( $1\sigma$  errors, dotted lines) of the differences between the measured values and the input values of the mean velocity  $V_{\text{in}}$  and the velocity dispersion  $\sigma_{\text{in}}$ . The bottom panels show the same lines for the recovered values of  $h_3$  and  $h_4$ , compared to the input values (dashed line). In the range of our observations  $\sigma \gtrsim 130 \text{ km s}^{-1}$  the recovered values are virtually unbiased.

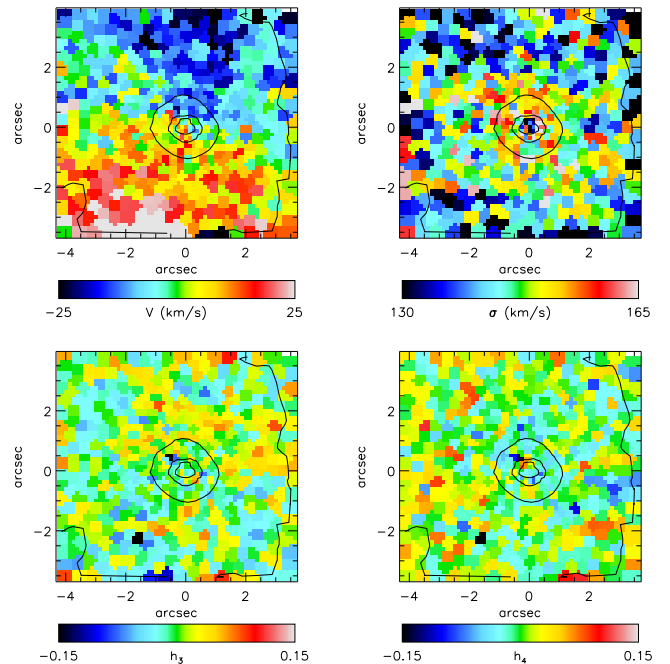


**Figure 3.** Voronoi binned stellar kinematics from the SINFONI 250mas observations. The four panels show the mean velocity  $V$ , the velocity dispersion  $\sigma$  and the two Gauss-Hermite moments  $h_3$  and  $h_4$ . Overlaid are the contours of the surface brightness derived from the reconstructed image, in 1 mag intervals. North is up and East is to the left.

ilar case of gas versus stars counter-rotation observed in the nucleus of the spiral galaxy NGC 5953 (Falcón-Barroso et al. 2006). In that case the nuclear gas rotation is associated to evidence of young stars which co-rotate with the gas and counter-rotate with respect to the outer part of the galaxy.

<sup>4</sup> Available from <http://www-astro.physics.ox.ac.uk/~mxc/cena09>.

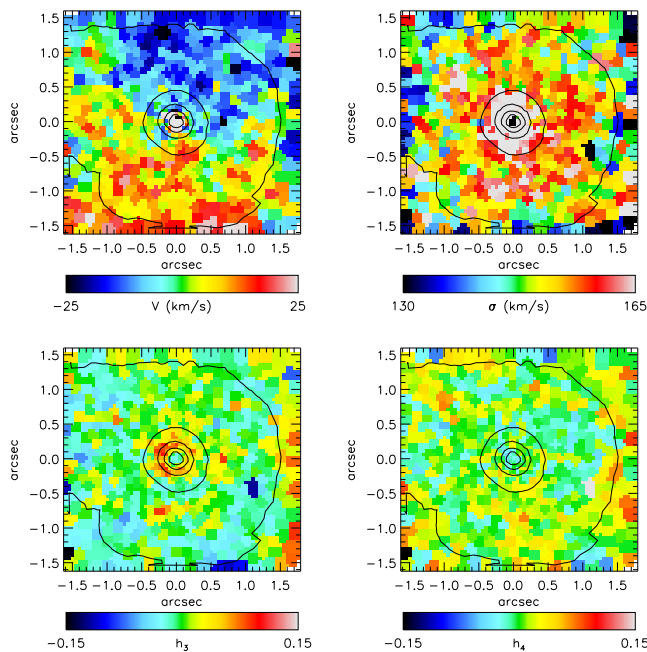


**Figure 4.** Same as in Fig. 3 for the SINFONI 100mas observations. The color levels are the same in this figure and in Fig. 3.

## 2.4 Contribution from the non-thermal nucleus

In the case of Cen A adopting a fixed template becomes important very close to the center, due to the presence of the non-thermal nucleus (Marconi et al. 2000). At radii where the nucleus dominates, the stellar absorptions are diluted, resulting in a strong decrease in the observed line-strength  $\gamma$ . Due to the strong correlation between  $\gamma$  and the stellar velocity dispersion  $\sigma$  (section 2.2 of van der Marel & Franx 1993), an inaccurate modeling of the non-thermal dilution can cause large errors in the measured  $\sigma$ . Similarly the rise in the non-thermal continuum could be incorrectly interpreted as a variation of the stellar population, requiring a change in the stellar template mix and also producing an error in  $\sigma$ . As there is no evidence for a sudden change in the population in the nucleus of Cen A the safest choice is to assume the stellar template is fixed and to model the non-thermal continuum via additive polynomials in pPXF. Additive polynomial still allow for low-order variations in the stellar line-strength and account for possible instrumental effects. This approach allows the  $\sigma$  to be reliably extracted in the high-resolution 100mas observations down to  $R \gtrsim 0''.2$ , before the photon noise of the nucleus eliminates all stellar information from the spectra.

As an illustration of the importance of taking the non-thermal continuum accurately into account in the kinematic extraction, in Fig. 5 we show the best fit with pPXF, using a Gaussian LOSVD, to the spectra extracted at different radii from the 100mas SINFONI data. We also performed separate fits including the Gauss-Hermite parameters  $h_3$  and  $h_4$ . In the range  $0''.3$ – $1''$ , where we can trust our extraction, the LOSVD is essentially consistent with a Gaussian as  $h_4 = -0.02 \pm 0.03$ , in agreement with Fig. 4. The high  $S/N$  spectra in these plots were obtained by co-adding all the spectra within circular annuli of one pixel width ( $0''.05$ ). The standard kinematics extraction approach for this paper consists of modeling the observed spectrum as the sum of a convolved fixed optimal template plus a fourth degree additive polynomial. To test the sensitivity of the measured  $\sigma$  to the details of the extraction, especially in

the critical continuum-dominated nuclear region, we compared our standard approach with others using different options in the pPXF routine: (i) We use a first degree polynomial; (ii) We fit the optimal template at each radius using our 11 stars; (iii) we use as template a single M5III star; (iv) We include in the fit the additive contribution of a scaled version of the nuclear non-thermal spectrum (as described in Kelson et al. 2000, to subtract the sky spectrum). All these four approaches give dispersion profiles which agree within the statistical errors for  $R > 0''.2$ .

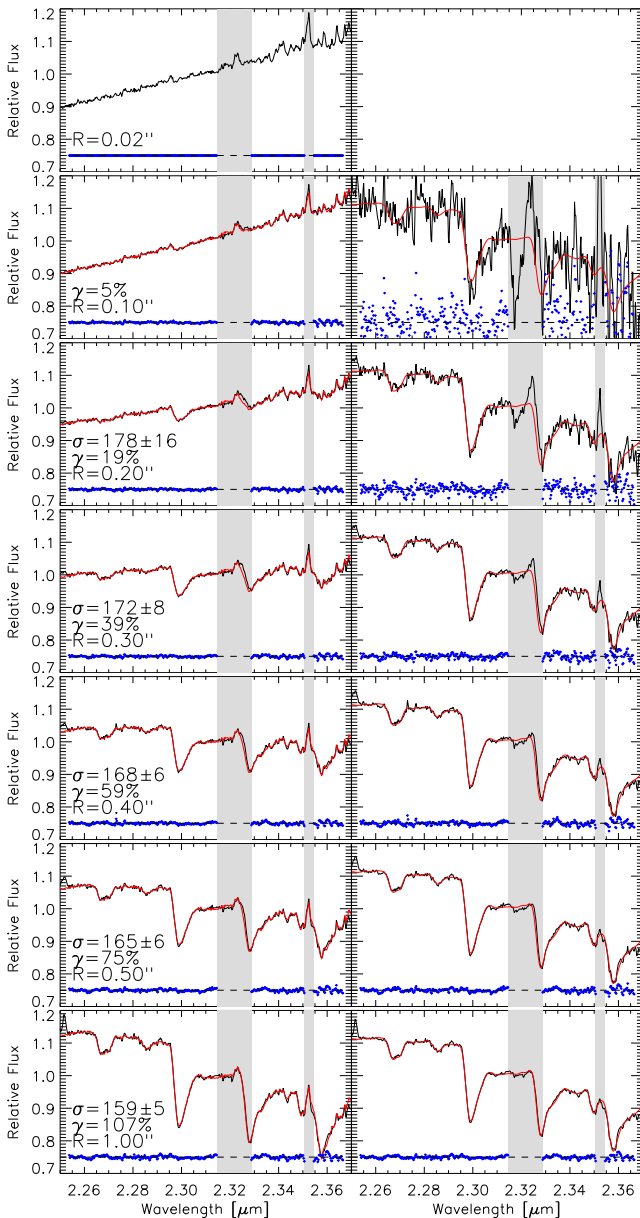
The last approach is the one which produces the best fit and describes almost every details of the observations. This is the one we show in Fig. 5. We also give in the plots the line-strength  $\gamma$ , defined as the ratio between the mean flux within the fitted range in the observed Cen A spectrum, and the flux contributed by the best fitting stellar template alone in the same range. At  $R \lesssim 0''.2$  the non-thermal source dominates and the spectrum shows a nearly linear trend. At  $R \approx 0''.2$  it becomes possible to estimate the velocity dispersion, however the stars still contribute only 19% of the flux in the observed spectrum, the statistical errors are large and the determination is still affected by large systematic uncertainties. At this radius the measured  $\sigma$  is sensitive to the details of the extraction. Only at larger radii the kinematics can be reliably extracted and will be included in our models.

Fig. 5 shows that the non-thermal continuum is still present in the spectra at the 25% level at  $R \approx 0''.5$ . The effect of the non stellar continuum is still clearly visible in the varying slope of the spectrum. Still at all radii the stellar spectrum is well approximated by the fixed convolved template, once the continuum is removed (right column of Fig. 5). To better quantify the extent of the dilution due to the central non-thermal continuum Fig. 6 shows the surface brightness profile  $I(R)$  measured from the reconstructed image of the 100mas data cube, together with the radial profile of the pure stellar contribution, estimated as  $\Sigma(R) = I(R)\gamma(R)$  from the result of the pPXF fit in the individual bins (see van der Marel 1994 for a similar analysis on the non-thermal nucleus of M 87). The plot shows that the underlying galaxy profile is smooth and well approximated by a shallow power-law  $\Sigma(R) \propto R^{-0.22}$ , as expected in a ‘core’ elliptical (Lauer et al. 1995; Marconi et al. 2001). This confirms that the observed radial spectral variation is consistent with being entirely due to the PSF effect and not to an intrinsic change in the stellar population. The measurement of  $\gamma(R)$  from the spectra allows for an extremely accurate determination of the halo of the PSF, which would be difficult to disentangle from the underlying galaxy via photometry alone.

## 3 STELLAR DYNAMICAL MODELING

### 3.1 Geometry of the stellar spheroid

Cen A appears very round on the sky and shows little rotation within one  $R_e$ . Wilkinson et al. (1986) mapped the full velocity field of Cen A with 71 slit positions out to  $100''$  from the nucleus. They found a maximum rotation of around  $40 \text{ km s}^{-1}$  roughly along the direction of the major axis at  $\text{PA}_{\text{kin}} \approx 35^\circ$ . Silge et al. (2005) find a comparable maximum rotation of about  $20 \text{ km s}^{-1}$  within  $40''$ . Adopting a luminosity-weighted dispersion  $\sigma_e \approx 138 \text{ km s}^{-1}$  (Silge et al. 2005), the amount of rotation can be quantified by the parameter  $V_{\text{max}}/\sigma_0 \approx 0.29$  (Binney 1978). From the empirical relation  $(V/\sigma)_e \approx 0.57 (V_{\text{max}}/\sigma_0)$  (equation [23] of Cappellari et al. 2007), we estimate for Cen A  $(V/\sigma)_e \approx 0.17$  (Binney 2005). The ellipticity of the galaxy within  $1R_e$ , measured from 2MASS  $K$ -band photometry, is very small  $\epsilon \lesssim 0.05$



**Figure 5.** Radial variation in the spectrum of Cen A in the 100mas SINFONI observations. *Left Column:* Different panels show the observed spectra (black solid line) obtained by co-adding the spectra of the spaxels contained within circular annuli of radius  $R$  and one pixel width ( $0''.05$ ). The best-fitting pPXF model (red solid line) consists of the stellar template (Fig. 1) convolved with a Gaussian LOSVD plus a fourth degree additive polynomial, plus a scaled copy of the non-thermal nuclear spectrum (top panel). The residuals are shown at the bottom of each panel with the blue dots. The value  $\gamma > 100\%$  at  $R = 1''$  is likely due to a small difference in the line strength of the stellar spectrum, or in the sky subtraction, with respect to the adopted optimal template. Emission from the [CaVIII] line at  $2.32\mu\text{m}$  and the  $\text{H}_2$  line at  $2.35\mu\text{m}$  were excluded from the fits (grey areas). These lines are prominent also outside the nucleus and cannot be properly subtracted by our model. *Right Column:* The convolved optimal template (red solid line) is compared to the observed spectrum after subtraction of the nuclear spectrum and polynomial contributions (black solid line). The blue dots show the residuals.

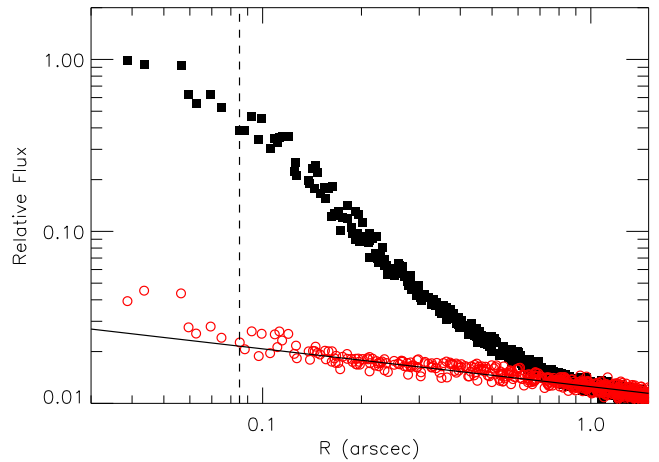


**Figure 6.** The radial surface brightness profile  $I(R)$  as measured from the individual pixels in the SINFONI 100mas scale (filled squares) is compared to the estimated profile of the stellar light  $\Sigma(R) = I(R)\gamma(R)$  (red open circles). As expected for a normal galaxy profile, the underlying stellar light profile is smooth and well approximated by a power-law  $\Sigma(R) \propto R^{-0.22}$  (solid line). The dashed vertical line marks the radius where the PSF has reached 50% of its peak value.

(Silge et al. 2005). These measured values seem to place Cen A on the region of the face-on fast rotator early-type galaxies on the  $(V/\sigma, \varepsilon)$  diagram (figure 11 of Cappellari et al. 2007).

Although the ellipticity of Cen A remains low  $\varepsilon \lesssim 0.1$  out to about  $3R_e$ , a well-defined photometric PA can still be determined. The major axis that we measure from the inertia ellipsoid of the surface brightness on the 2MASS  $K$ -band photometry (Jarrett et al. 2003) at large radii is  $\text{PA}_{\text{phot}} = 35^\circ \pm 3^\circ$  (East of North). The axis of maximum rotation that we determine from our 250mas SINFONI data is quite different at  $\text{PA}_{\text{kin}} = 167^\circ \pm 8^\circ$  (Section 2.3). The sense of stellar rotation that we measure is in support to the determination by Wilkinson et al. (1986), and our accurate  $\text{PA}_{\text{kin}}$  is probably consistent with their determination, given their large uncertainties.

The strong kinematical misalignment of  $\sim 48^\circ$  is an indication that the galaxy is certainly not an axisymmetric object. This is consistent with the strong twist in the kinematical position angle of the planetary nebula system at large radii (Hui et al. 1995; Peng et al. 2004b). However the galaxy is unlikely to be well described by a stationary triaxial geometry either. In fact at radii where Cen A starts to appear more elongated, its surface brightness is dominated by stellar shells, which constitute the relics of a recent accretion event and are likely associated with the polar geometry of the strong dust lane which crosses the galaxy nucleus (Malin et al. 1983; Quillen et al. 1993; Israel 1998). This shows that at those radii the galaxy has not reached an equilibrium configuration. The relatively low but ordered rotation near the nucleus, the presence of prominent stellar shells at large radii and the strong kinematical misalignment of Cen A are reminiscent of the fast rotator S0 NGC 474 in Emsellem et al. (2007). However only much more extended integral-field observations in the near-infrared, sampling up to  $1R_e$ , could conclusively reveal the dynamical status of the central regions of Cen A.

At different radii the galaxy is expected to reach an equilibrium configuration in very different time scales, starting from the center. We estimated the circular velocity  $V_c$  of Cen A from the Multi-Gaussian Expansion (MGE; Emsellem et al. 1994)

parametrization of its  $K$ -band surface brightness tabulated in Häring-Neumayer et al. (2006) and the best fitting mass-to-light ratio  $M/L$  we derive in this paper. It is nearly flat over two orders of magnitude in radius  $V_c \sim 200 \text{ km s}^{-1}$  from  $4''$ – $400''$ . This implies that at the edge of our SINFONI observations ( $R \sim 4''$ ) the characteristic orbital period is  $T \sim 2 \text{ Myr}$ , while it is  $T \sim 0.2 \text{ Gyr}$  at large radii where the stellar body starts to become more elongated and shells are still visible. The very short orbital period in the central regions, where the galaxy is nearly circular in projection, suggests that it has already reached an equilibrium configuration there. Given that the kinematics at a certain projected radius  $R$  is mostly influenced by stellar orbits having that same characteristic radius  $R$  (Krajnović et al. 2005), this justifies the use of stationary dynamical models to study the central dynamics of Cen A, even though the galaxy is still dynamically evolving at larger radii.

For this paper we will construct two types of models, to test the sensitivity of the  $M_{\text{BH}}$  estimate to the assumed geometry and dynamics. We build (i) an axisymmetric orbit-based model, to reproduce in detail the kinematic observations, and (ii) a simple anisotropic spherical Jeans model to qualitatively check the  $M_{\text{BH}}$  determination.

### 3.2 Axisymmetric three-integral models

Our axisymmetric three-integral dynamical model is based on Schwarzschild (1979) numerical orbit-superposition method. This has become the current standard for all  $M_{\text{BH}}$  determinations from the stellar kinematics, available in the literature from different groups (e.g. van der Marel et al. 1998; Gebhardt et al. 2003; Valluri et al. 2005). The axisymmetric implementation we use, the orbital ‘dithering’ and the setup we employ, are described in detail in Cappellari et al. (2006). The relatively limited spatial extension of the integral-field data, and the likely lack of equilibrium at large radii, does not justify the use of more general triaxial models (de Lorenzi et al. 2007; van den Bosch et al. 2008).

Our dynamical model assumes constant  $M/L$ . This is likely a good approximation in the central regions ( $R \lesssim R_e$ ) of Cen A, where dark matter is expected to contribute only a small fraction of the mass (Hui et al. 1995; Peng et al. 2004b) as observed via dynamics or gravitational lensing in larger samples of early-type galaxies (Gerhard et al. 2001; Rusin et al. 2003; Cappellari et al. 2006; Koopmans et al. 2006; Thomas et al. 2007; Bolton et al. 2008). The model still allows for dark matter in the form of a constant shift in the global  $M/L$ . Our model assumes an MGE parametrization for the  $K$ -band surface brightness of Cen A using the values tabulated in Häring-Neumayer et al. (2006).

The models are fitted to our integral-field SINFONI 100mas (with AO correction) and 250mas kinematics in the central regions ( $R \lesssim 4''$ ), and to the two-slits GNIRS kinematics of Silge et al. (2005) at larger radii ( $R \lesssim 40''$ ). For  $R < 1''$  we only used the SINFONI 100mas data in the fit, not to spoil the information contained in the high-resolution AO-assisted observations with the seeing-limited 250mas ones. Similarly we do not fit the GNIRS kinematics for  $R < 3''.5$ , where we have higher quality SINFONI data. As the models are bi-symmetric by construction, the SINFONI kinematics were bi-symmetrized before the fit along  $\text{PA}_{\text{kin}} = 167^\circ$ . For all datasets we fit, and we compute the predictions, for the Gauss-Hermite moments up to  $h_3$ – $h_6$ , where  $h_3$  and  $h_4$  are the measured values, while we set  $h_5 = h_6 = 0 \pm 0.3$  ( $1\sigma$  errors). This is done to include in the model the additional observational constraint that extreme values for the high-order moments are never observed (see two extreme examples in fig. 4 of Cappellari et al. 2007).

We constructed a set of models with slightly different geometries to test the variation in the recovered  $M_{\text{BH}}$ : (i) An edge-on model ( $i = 90^\circ$ ); (ii) An edge-on model with the major axis GNIRS kinematics aligned with  $\text{PA}_{\text{kin}} = 167^\circ$ . In this case we set  $V = h_3 = 0$  for the GNIRS minor axis data; (iii) An edge-on model with ‘circularized’ GNIRS kinematics. Here we assumed the  $\sigma$  and  $h_4$  field have circular symmetry, and a profile given by the average of the two slits. We fitted the  $\sigma$  and  $h_4$  GNIRS kinematics along five polar sectors, covering the whole galaxy from the major to the minor axis, and not just the observed major/minor axes. (iv) Same as model [ii], but with  $i = 60^\circ$ , which is the average inclination for random orientations; (v) Same as model [ii], but with  $i = 45^\circ$ . All these models are expected to produce similar results given that the differences between the major and minor axis GNIRS kinematics are almost at the level of the measurement errors, and given that Cen A is so close to circular within the region where we have kinematics, that for large ranges of inclination the intrinsic density is essentially spherical. We find that indeed all these models produce BH mass estimates well within the errors, and have similar uncertainties. The orbital distribution of all the models is also nearly the same. For this reason we will not present the individual results. Instead for all our figures below we adopt as representative the model (ii).

The two best-fitting parameters of the model,  $M_{\text{BH}}$  and  $M/L$ , were determined as follows. After an initial approximate search for the best fitting parameters using isotropic Jeans models (Section 3.3), we computed a set of orbit libraries, each consisting of 444,528 individual orbits, at our first guess for  $M/L$ . For each set the  $M_{\text{BH}}$  was sampled linearly in  $u = \sinh(M_{\text{BH}}/M_{\text{BH, best}})$ , where  $M_{\text{BH, best}}$  is our first guess for  $M_{\text{BH}}$ . We then scaled the velocities of the orbits to compute models at different  $M/L$  (van der Marel et al. 1998). In the fit we use a modest amount of regularization  $\Delta = 10$  (see van der Marel et al. 1998, for a definition). The contours of the resulting  $\chi^2$ , which describe the agreement between the models and the data, are shown in Fig. 7. The best fitting BH has mass  $M_{\text{BH}} = (5.5 \pm 3.0) \times 10^7 M_\odot$ , where the  $3\sigma$  error bars are marginalized over the  $M/L$  and correspond to one degree-of-freedom ( $\Delta\chi^2 = 9$ ). The corresponding best fitting  $K$ -band  $M/L = (0.65 \pm 0.15) M_\odot/L_\odot$ .

The data-model comparison for our best fitting model are shown in Fig. 8. All the significant features of the data are reproduced in detail by the model, for the two SINFONI datasets. Unsurprisingly the GNIRS long-slit data are also reproduced in detail (not shown). Although we only have observations along two slits, we still predict the model kinematics over a full quadrant, to verify that the model does not contain un-physical features or sharp discontinuities, which are never observed in real galaxies (Emsellem et al. 2004).

The orbital anisotropy of our best fitting model is shown in Fig. 9. We plot the ratio  $\sigma_r/\sigma_t$  between the radial velocity dispersion  $\sigma_r$  and the tangential one defined as  $\sigma_t^2 = (\sigma_\phi^2 + \sigma_\theta^2)/2$ . Here  $\sigma_\phi$  includes only random motion and not ordered rotation, so that an isotropic system has  $\sigma_r/\sigma_t = 1$ , and  $(r, \theta, \phi)$  are the standard spherical coordinates. We also plot for reference the radius at which the total luminous mass in the MGE model is equal to  $M_{\text{BH}}$ , for our best fitting  $M/L$  and  $M_{\text{BH}}$  values. The derived value is  $R_{\text{BH}} = 0''.70$ , which is very close to the usual practical definition of the BH radius of influence  $R_{\text{BH}} = GM_{\text{BH}}/\sigma_e^2 = 0''.68$ , for  $\sigma_e = 138 \text{ km s}^{-1}$  (see also Marconi et al. 2006). Also shown is the break radius  $R_b = 3''.9$  of a Nuker-law (Lauer et al. 1995) fit to the  $K$ -band HST photometry (Marconi et al. 2000). Both radii are very well resolved by the observations, which then allow the

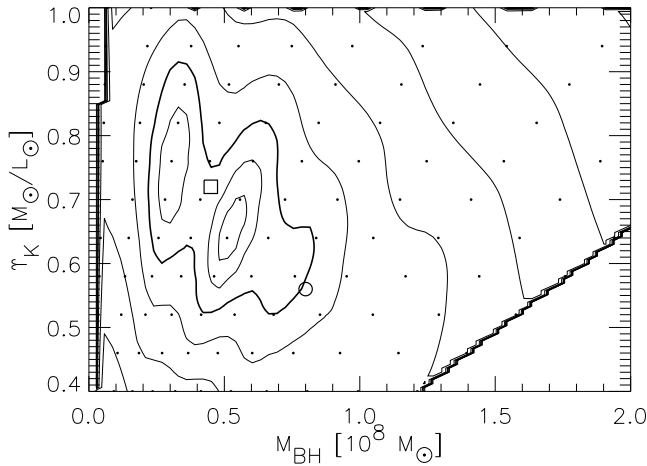


**Figure 7.** Determination of the best fitting parameters. The contours of the  $\chi^2$ , which describes the agreement between the data and the model, are plotted as a function of  $M_{\text{BH}}$  and  $K$ -band  $M/L$ . The lowest levels show the  $\Delta\chi^2 = \chi^2 - \chi_{\text{min}}^2$  which correspond to confidence levels of 1, 2 and  $3\sigma$  (thick contour), for one parameter. Additional contours are separated by factors of two in  $\Delta\chi^2$ . The open square marks the best fitting  $M_{\text{BH}}$  derived from the gas kinematics by Neumayer et al. (2007). The open circle is the best fitting isotropic model from Section 3.3. The small dots are the locations of the models that were run, while the  $\chi^2$  was interpolated at other locations.

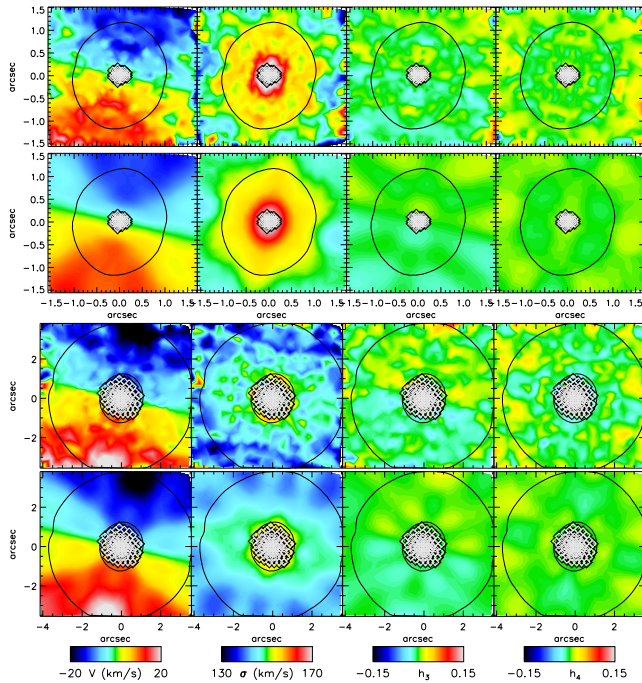


**Figure 8.** Data-model comparison for the best fitting three integral model. *Top two panels:* The top row shows the symmetrized and linearly interpolated 100mas SINFONI data of Fig. 4. The second row show the best fitting dynamical model predictions. The central bins that were excluded from the fit are shown with the white diamonds. *Bottom two panels:* Same as in the top two panels, for the 250mas SINFONI kinematics. For each quantity the color scale is the same in the two instrumental configurations.

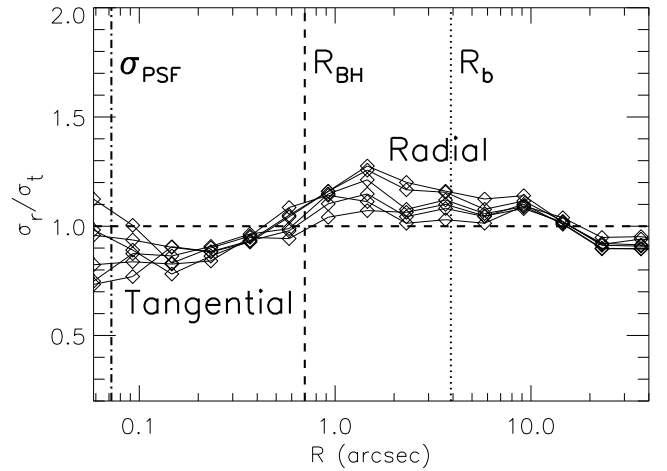


**Figure 9.** Anisotropy variation. The diamonds, connected with solid lines, show the anisotropy  $\sigma_r/\sigma_t$  (see text for a definition) measured at different polar angles, from the equatorial plane to the symmetry axis, in the galaxy meridional plane. As the model is nearly spherical, the differences at a given radius, provide a rough indication of the model uncertainties. Also shown are the break radius (or core radius)  $R_b$ , the BH radius of influence  $R_{\text{BH}}$  and the  $\sigma$  of the best fitting Gaussian model of the SINFONI 100mas PSF.

nuclear orbital distribution to be robustly recovered. The velocity ellipsoid appears to deviate from a sphere (isotropy) by just 15% in the whole range where we have kinematics. This is just above the errors of 5% in this determination (Cappellari et al. 2007). The main significant trend is a decrease in the  $\sigma_r/\sigma_t$  ratio inside  $R_{\text{BH}}$ , but no sharp transition is seen near  $R_b$ .

### 3.3 Anisotropic spherical Jeans models

In the previous section we used general axisymmetric Schwarzschild models to determine  $M_{\text{BH}}$  and to derive the anisotropy profile in the nucleus of Cen A. In this section we use simpler anisotropic spherical Jeans models to test the reliability of these modeling results.

In the past 25 years the dynamical models of galaxies have evolved from simple spherical models based on the Jeans equations (Binney & Mamon 1982) to quite general orbit- or particle-based numerical techniques with spherical (Richstone & Tremaine 1988; Rix et al. 1997), axisymmetric (e.g. van der Marel et al. 1998) or triaxial geometry (de Lorenzi et al. 2007; van den Bosch et al. 2008). Contrary to the models based on the Jeans equations, which can generally be solved and tested to machine precision, the results of the more general models are sensitive to the numerical implementation details and more difficult to test thoroughly. Moreover the complexity of the general models often prevents a qualitative assessment of the results, which sometimes have to rely entirely on subtle details of the kinematics (e.g. fig. 2 of Gebhardt et al. 2003 or fig. 7 of Nowak et al. 2007).

One way to gain confidence in the  $M_{\text{BH}}$  determinations and the recovered anisotropy is by comparing them with the simpler Jeans models (van der Marel et al. 1998; Cretton & van den Bosch 1999). These models are based on a completely different set of assumptions and do not suffer from possible incompleteness in the sampling of the orbit library or from limited kinematic coverage. To test our best fitting  $M_{\text{BH}}$  and  $M/L$  and the corresponding recovered anisotropy profile of Fig. 9 we use the Jeans Anisotropic MGE (JAM) package<sup>3</sup> of Cappellari (2008). The method allows

one to compute the predicted second moments, projected onto the sky plane, for a model with a variable anisotropy profile, via a quick and accurate single numerical quadrature. Given that our standard model of Cen A is intrinsically close to spherical, we use the spherical formalism of equation (50) of Cappellari (2008).

We construct a spherical model having the same MGE surface brightness as our Schwarzschild model, but we set the axial ratios of all the Gaussians  $q'_i = 1$ . We assume the same anisotropy profile of our best fitting Schwarzschild model of Section 3.2, with the same  $M_{\text{BH}}$  and  $M/L$ . The method allows for a different anisotropy  $\beta = 1 - \sigma_\theta^2/\sigma_r^2$  to be assigned to different Gaussian components of the MGE model. In practice we assign an anisotropy  $\beta = 0.2$  (radial anisotropy) to the Gaussians with  $0''.5 < \sigma_i < 10''$  and an anisotropy  $\beta = -0.35$  (tangential anisotropy) to the remaining Gaussians. Although  $\beta$  changes in a discontinuous fashion for the different MGE Gaussians, the resulting  $\beta$  profile is smooth. In fact the Gaussians overlap with each other and the  $\beta$  at a certain spatial position is a luminosity-weighted sum of the  $\beta$  of the individual components.

This anisotropic model, mimicking the best-fitting three-integral model, is shown with the solid line in the top panel of Fig. 10. Although the model is not by itself a fit to the data, it provides a remarkably accurate description of the observed and radially-averaged SINFONI and GNIRS (outside  $R \gtrsim 1''$ ) second velocity moments  $V_{\text{rms}} \equiv \sqrt{V^2 + \sigma^2}$ . We ignore the  $h_4$  Gauss-Hermite moment in the  $V_{\text{rms}}$  estimation, as it is essentially zero within the errors. The purely Gaussian LOSVD extraction of Fig. 5 gives consistent  $V_{\text{rms}}$  values within the errors. This test shows that the best-fitting discrete Schwarzschild's numerical representation of Cen A is an excellent approximation for the continuum limit represented by the Jeans model. It provides a strong confirmation for the recovered anisotropy profile and the need for tangential anisotropy in the nucleus of Cen A. We also show in Fig. 10, with the two dashed lines, the Jeans predictions for two  $M_{\text{BH}}$  corresponding to the  $3\sigma$  upper and lower confidence limits of the Schwarzschild model. They show that, as expected, inside  $R \lesssim 1''$  the data are very sensitive to a change in  $M_{\text{BH}}$  at the level of the quoted errors.

The dotted line shows the model prediction, still with the same  $\beta$  profile as for the previous models, for  $M_{\text{BH}} = 2 \times 10^8 M_\odot$ . This is the best fitting value determined by Silge et al. (2005) from the GNIRS data. This model has a much steeper  $V_{\text{rms}}$  profile near the center, which seems to qualitatively reproduce the steeper rise of the  $V_{\text{rms}}$  in the GNIRS data within  $R \lesssim 1$ . Unfortunately we cannot compare our Jeans models with the more nuclear GNIRS kinematics ( $R \lesssim 0''.5$ ). Those measurements have rather extreme  $h_4 \gtrsim 0.2$  values. In this case it becomes not possible to reliably translate the kinematics into a true  $V_{\text{rms}}$  value, as required by the Jeans equations. In fact when the Gauss-Hermite moments are large, the  $V_{\text{rms}}$  one can derive by formally integrating over the LOSVD is extremely sensitive to the wings of the LOSVD which are observationally not well constrained. For this reason we limit our comparison to the remaining values, for which  $h_4$  is consistent with zero within the  $1\sigma$  errors. Our comparison suggests that the  $\sim 4\times$  higher value for  $M_{\text{BH}}$  derived by those authors is not due to differences in the modeling, but more likely to the differences in the measured nuclear kinematics profile with GNIRS. A more conclusive evidence would require a full Schwarzschild model of the nuclear GNIRS data, which is outside the scope of this paper.

It is clear however that our SINFONI nuclear kinematics is not consistent with the GNIRS one of Silge et al. (2005) when  $R \lesssim 1''$ . Those authors measure larger  $\sigma$  values and especially strong  $h_4$  values in the nucleus, while we find  $h_4 \sim 0$  over the full field-of-view

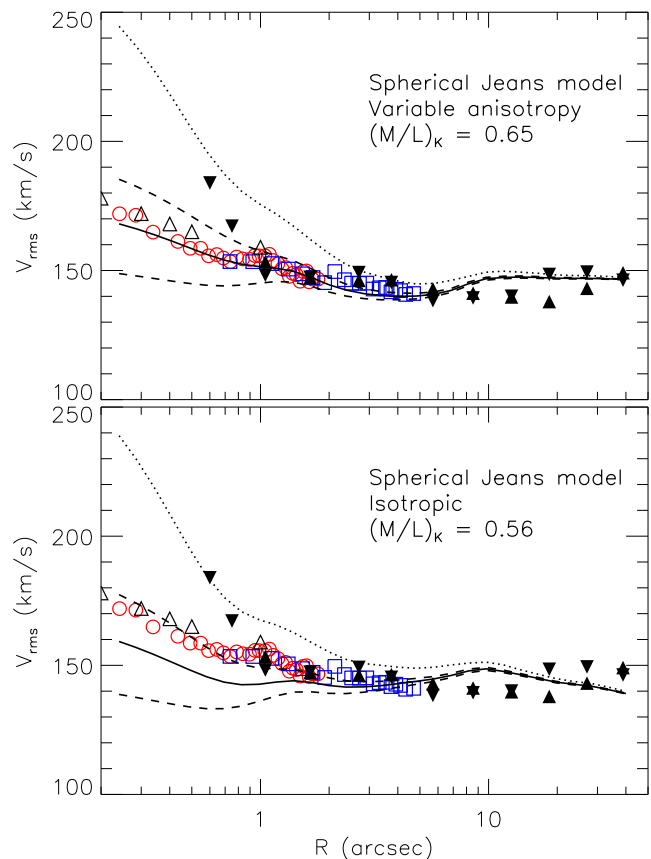


**Figure 10.** Spherical Jeans models. *Top Panel:* Our SINFONI observations of  $V_{\text{rms}} \equiv \sqrt{V^2 + \sigma^2}$  for the 100mas (red open circles) and 250mas scale (blue open squares), biweight averaged over circular annuli, are plotted as a function of the radius from the center of Cen A. This is the same kinematics presented in Fig. 3 4, which was used in the Schwarzschild models. We also show for comparison, as black open upward triangles, the  $\sigma$  measured in Fig. 5, assuming a purely Gaussian LOSVD. The corresponding GNIRS  $V_{\text{rms}}$  observations of Silge et al. (2005) along the major axis (filled downward triangle) and the minor axis (filled upward triangle), are also shown for  $R \gtrsim 0''.5$  (see text for a discussion of the discrepancy between the GNIRS and SINFONI data inside  $R \lesssim 1''$ ). These have been arbitrarily scaled up by 5% to match our data at  $R > 1''$  (see text). The solid line shows the prediction of a JAM model, having the best fitting  $M_{\text{BH}}$  and  $M/L$  derived from the Schwarzschild model of Fig. 7 and the corresponding anisotropy profile of Fig. 9. The model was convolved with the PSF of the 100mas observations. The two dashed lines have a  $M_{\text{BH}}$  corresponding to the upper and lower  $3\sigma$  errors in the Schwarzschild model. The dotted line has  $M_{\text{BH}} = 2 \times 10^8$ , corresponding to the best fitting value of Silge et al. (2005). *Bottom Panel:* Same as in the top panel, but assuming isotropy ( $\beta = 0$ ) for all the Jeans models. The  $M/L$  has been decreased to match the data at large radii.

(Fig. 4). The reasons for these differences are likely the following: (i) Our SINFONI data represent a significant improvement over the GNIRS one, both in  $S/N$  and in spatial resolution (compare fig. 6 of Silge et al. 2005 with the right column of our Fig. 5). The GNIRS data forced them to extract the kinematics inside  $R < 1''$  by fitting only the first CO band, while we could accurately fit all three CO bands from the SINFONI data, down to the limit where they disappear due to the rise of the non-thermal nucleus; (ii) We used different approaches for the subtraction of the non-thermal continuum. As discussed in detail in Section 2.4, a non accurate subtraction of the non-thermal contribution from the spectrum, leads directly to

an error in  $\sigma$ . We subtracted the non-thermal source with additive polynomials during the pPXF fit, so that both the kinematics and the continuum contribution are simultaneously optimized to fit the spectrum. Silge et al. (2005) instead removed the continuum based on a measure of CO line-strength and only subsequently fitted the kinematics on the continuum-free spectrum.

For comparison, in the bottom panel of Fig. 10, we show four spherical Jeans models with the same  $M_{\text{BH}}$  as in the top panel, but in this case assuming isotropy ( $\beta = 0$ ). The  $M/L$  was decreased to fit the data at large radii, where the BH contribution is minimal. A reasonable fit to the  $V_{\text{rms}}$  is obtained in this case at the upper limit  $M_{\text{BH}} = 8 \times 10^7 M_{\odot}$  of our Schwarzschild confidence interval. This general agreement confirms previous comparisons, showing that although general three-integral models are needed for accurate  $M_{\text{BH}}$  determinations, much simpler isotropic models, applied to the same data, provide a useful sanity-check for the determination (van der Marel et al. 1998; Cretton & van den Bosch 1999; Joseph et al. 2001; Verolme et al. 2002). These simple tests would be especially useful to give confidence in the  $M_{\text{BH}}$  determinations in critical cases, where  $R_{\text{BH}}$  is barely resolved and a determination of  $M_{\text{BH}}$  seems at the limit of what is possible with current technologies (e.g. Davies et al. 2006; Nowak et al. 2007, 2008).

Gebhardt (2004) compared the  $M_{\text{BH}}$  determinations between two-integral and three-integral models for 10 galaxies and found that, even using seeing-limited ground-based data, the two-integral  $M_{\text{BH}}$  of Magorrian et al. (1998) are systematically too high by just a factor  $\sim 2$ , with respect to more recent three-integral models, based on high-resolution HST observations. It would be interesting to perform a similar type of comparison, but using the same data for both anisotropic Jeans and Schwarzschild models.

The reason for the reasonable agreement between the simpler and the more general models is likely due to the fact that many real galaxies do not ‘utilize’ all the freedom in the orbital distribution that would be required to produce more dramatic disagreements, and do not deviate very strongly from being isotropic in their centers (e.g. Verolme et al. 2002; Gebhardt et al. 2003; Shapiro et al. 2006). This is certainly true for the results presented in this paper.

#### 4 DISCUSSION

Our determination, using the stellar kinematics, for the BH mass in the center of Cen A  $M_{\text{BH}} = (5.5 \pm 3.0) \times 10^7 M_{\odot}$  agrees very well with the determination  $M_{\text{BH}} = (4.9 \pm 1.4) \times 10^7 M_{\odot}$  we performed using the gas kinematics in Neumayer et al. (2007) from the same SINFONI data. This gas-stars  $M_{\text{BH}}$  comparison constitutes one of the most robust and accurate ones, due to a very well resolved BH sphere of influence ( $R_{\text{BH}} \approx 0''.70$  compared to a PSF FWHM  $\approx 0''.17$ ) and thanks to the use of high-resolution integral-field data for both kinematical tracers. Comparable and equally successful comparisons were done by Shapiro et al. (2006) and Siopis et al. (2008), while a less good agreement was found in Cappellari et al. (2002), likely due to the disturbed gas kinematics.

In Neumayer et al. (2007) we made a detailed comparison with all the numerous previous  $M_{\text{BH}}$  determinations for Cen A (Marconi et al. 2001, 2006; Silge et al. 2005; Häring-Neumayer et al. 2006; Krajnović et al. 2007). In summary the only significant disagreement in  $M_{\text{BH}}$  is with the previous stellar  $M_{\text{BH}}$  determination by Silge et al. (2005). In Section 3.3 we showed that the disagreement is likely caused by a difference in the data quality and in the treatment of the contribution from the central non-thermal continuum in the kinematic extraction. It is not due

to differences in the details of the modeling methods. As shown in Neumayer et al. (2007), with our new gas and stars  $M_{\text{BH}}$  determination Cen A lies within the errors on the  $M_{\text{BH}} - \sigma$  relation as given by either Tremaine et al. (2002) or Ferrarese & Ford (2005).

The value  $(M/L)_K = 0.65$  is well consistent with what one would expect from a  $\sim 7$  Gyr luminosity-weighted age of the stellar population of Cen A, almost independently of the assumed near-solar metallicity. This adopts the Kroupa (2001) *normalization* of the initial mass function (IMF) and uses the population models of Maraston (2005). These population models include a proper treatment of the TP-AGB stars which is essential for a reliable prediction of the near-infrared flux and  $(M/L)_K$ . The  $(M/L)_K$  of the stellar population would decrease to 50% of the observed dynamical value if Cen A had a mean age of  $\sim 3$  Gyr. In that case dark-matter would be required to explain the observations. However the younger age is at the lower extreme of the estimated age of 3–8 Gyr, for the main body of Cen A, from the analysis of its globular cluster system (Peng et al. 2004a). Adopting the normalization of the Salpeter (1955) IMF, the mean age of Cen A would have to be lower than  $\sim 3$  Gyr for the population  $(M/L)_K$  not to over-predict the dynamical one. However this IMF normalization has been shown to be inconsistent with the observed dynamical  $M/L$  of early-type galaxies as a class (Cappellari et al. 2006; see de Jong & Bell 2007 for a review).

Cen A possesses a clear core in the luminosity profile, with a break from a shallow central slope to a steeper outer one at a radius  $R_b \approx 3''.9$  (Marconi et al. 2000), which is extremely well resolved by our kinematics. Every galaxy spheroid seems to host a supermassive BH (Magorrian et al. 1998; Ferrarese & Merritt 2000; Gebhardt et al. 2000), and galaxies are expected to form by mergers. These cores have been interpreted as due to the scouring of the galaxy profile due to the ejection of stars in radial orbits passing close to the BH binary which forms shortly after mergers (Faber et al. 1997; Quinlan & Hernquist 1997; Milosavljević & Merritt 2001). The models predicts that the anisotropy should show a bias towards tangential orbits inside  $R_b$ .

To test this prediction, in this paper we present the recovered stellar anisotropy profile  $\sigma_r/\sigma_t$  for Cen A (Fig. 9). The profile is to first order flat around the value  $\sigma_r/\sigma_t \approx 1$ . The maximum deviations of the velocity ellipsoid from a sphere (isotropy) are on the order of 15%. The profile shows no sudden bias towards tangential orbits inside  $R_b$ , while a tangential bias appears only inside  $R_{\text{BH}}$ . This profile seems typical of the few nuclear anisotropy profiles that have been published so far using integral-field observations or spherical models (the only cases for which the orbital distribution can be robustly recovered): M32 (Verolme et al. 2002), M87 (Cappellari & McDermid 2005), NGC 3379 (Shapiro et al. 2006), NGC 1399 (Houghton et al. 2006; Gebhardt et al. 2007). A similar anisotropy trend was observed with high-resolution HST long-slit data by Gebhardt et al. (2003), although in that case the profiles appear more noisy.

Although the predicted tangential bias is observed, its size does not seem related to that of the core. So these anisotropy determinations would not seem to support the scenario in which the cores have been produced by the core-scouring mechanism. However a big caveat is that the current simulations are not entirely realistic: they only consider binary mergers of cusp galaxies which are initially isotropic. Now that high-quality anisotropy measurements are starting to appear, it would be valuable if the numerical simulations could revisit their predictions in a more cosmological motivated setting, considering sequences of multiple mergers. For

the moment we must refrain from making firm statements on what our anisotropy profile implies for BH formation.

## 5 SUMMARY

We present a determination of the mass of the supermassive BH in the nucleus of the nearby elliptical galaxy Cen A, using high spatial resolution integral-field observations of the stellar kinematics, combined with large-scale long-slit kinematics. Our high-resolution observations were obtained in the near infrared  $K$ -band with SINFONI on the VLT, using adaptive optics to correct for the blurring effect of the atmosphere. The PSF of our data has a close to diffraction-limited resolution of  $0''.17$  FWHM and very high  $S/N \gtrsim 80$  per spectral pixel. We discuss the extraction of the stellar kinematics, with particular emphasis on the treatment of the non-thermal continuum coming from the nucleus of Cen A, which contaminates the central stellar spectra.

We use a standard three-integral axisymmetric numerical orbit-superposition model to determine the mass of the supermassive BH, which turns out to be  $M_{\text{BH}} = (5.5 \pm 3.0) \times 10^7 M_{\odot}$ . This value is in good agreement with our previous accurate determination  $M_{\text{BH}} = (4.9 \pm 1.4) \times 10^7 M_{\odot}$ , obtained from the gas kinematics extracted from the same SINFONI data (Neumayer et al. 2007). It is also in agreement with the recent analysis of the HST gas kinematics by Marconi et al. (2006), and with other similar, but with lower spatial resolution,  $M_{\text{BH}}$  determinations. This mass is consistent with the prediction of the  $M_{\text{BH}} - \sigma$  relation of either Tremaine et al. (2002) or Ferrarese & Ford (2005). We carefully test the  $M_{\text{BH}}$  and anisotropy recovery from our three-integral stellar modeling using simple anisotropic spherical MGE Jeans models. We find very good consistency between the two different approaches.

We study the nuclear orbital distribution of Cen A. In agreement with a few previous studies of other galaxies, we find a tangential bias in the anisotropy near the BH. However the size of the tangential region do not seem to be associated with that of the core radius  $R_b$  of the surface brightness profile, but has the size of the much smaller BH sphere of influence  $R_{\text{BH}}$ . This does not add support to the scenario in which galaxy cores are scoured by binary BHs. More realistic numerical simulations would be required for a comparison with the new accurate data and to draw conclusions from this observation.

## ACKNOWLEDGEMENTS

MC acknowledge support from a STFC Advanced Fellowship (PP/D005574/1). NN acknowledges support from the Christiane-Nüsslein-Volhard Foundation. JR acknowledges financial support from the Academy of Finland (project 8121122). We are grateful to the referee Karl Gebhardt for a thoughtful report, which improved the presentation of our work. Based on observations collected at the European Southern Observatory, Paranal, Chile, ESO Program 075.B-0490(A).

## REFERENCES

Aller M. C., Richstone D. O., 2007, *ApJ*, 665, 120  
 Baes M., Buyle P., Hau G. K. T., Dejonghe H., 2003, *MNRAS*, 341, L44  
 Bender R., Saglia R. P., Gerhard O. E., 1994, *MNRAS*, 269, 785

Binney J., 1978, *MNRAS*, 183, 501  
 Binney J., 2005, *MNRAS*, 363, 937  
 Binney J., Mamon G. A., 1982, *MNRAS*, 200, 361  
 Binney J., Tabor G., 1995, *MNRAS*, 276, 663  
 Bolton A. S., Treu T., Koopmans L. V. E., Gavazzi R., Moustakas L. A., Burles S., Schlegel D. J., Wayth R., 2008, *ApJ*, 684, 248  
 Bonnet H., et al. 2003, in Wizinowich P. L., Bonaccini D., eds, Adaptive Optical System Technologies II. Proc. SPIE Vol. 4839. pp 329–343  
 Bower R. G., Benson A. J., Malbon R., Helly J. C., Frenk C. S., Baugh C. M., Cole S., Lacey C. G., 2006, *MNRAS*, 370, 645  
 Cappellari M., 2008, *MNRAS*, 390, 71  
 Cappellari M., et al., 2006, *MNRAS*, 366, 1126  
 Cappellari M., Copin Y., 2003, *MNRAS*, 342, 345  
 Cappellari M., Emsellem E., 2004, *PASP*, 116, 138  
 Cappellari M., et al., 2007, *MNRAS*, 379, 418  
 Cappellari M., McDermid R. M., 2005, *Classical and Quantum Gravity*, 22, 347  
 Cappellari M., Verolme E. K., van der Marel R. P., Kleijn G. A. V., Illingworth G. D., Franx M., Carollo C. M., de Zeeuw P. T., 2002, *ApJ*, 578, 787  
 Cattaneo A., Dekel A., Devriendt J., Guiderdoni B., Blaizot J., 2006, *MNRAS*, 370, 1651  
 Ciotti L., Ostriker J. P., 1997, *ApJ*, 487, L105+  
 Cretton N., van den Bosch F. C., 1999, *ApJ*, 514, 704  
 Croton D. J., et al., 2006, *MNRAS*, 365, 11  
 Davies R. I., et al., 2006, *ApJ*, 646, 754  
 de Jong R. S., Bell E. F., 2007, *Comparing Dynamical and Stellar Population Mass-To-Light Ratio Estimates. Island Universes - Structure and Evolution of Disk Galaxies*, pp 107  
 de Lorenzi F., Debattista V. P., Gerhard O., Sambhus N., 2007, *MNRAS*, 376, 71  
 Di Matteo T., Springel V., Hernquist L., 2005, *Nature*, 433, 604  
 Eisenhauer F., et al. 2003a, in Iye M., Moorwood A. F. M., eds, Instrument Design and Performance for Optical/Infrared Ground-based Telescopes. Proc. SPIE Vol. 4841. pp 1548–1561  
 Eisenhauer F., et al. 2003b, *The Messenger*, 113, 17  
 Emsellem E., et al., 2007, *MNRAS*, 379, 401  
 Emsellem E., et al., 2004, *MNRAS*, 352, 721  
 Emsellem E., Monnet G., Bacon R., 1994, *A&A*, 285, 723  
 Faber S. M., et al. 1997, *AJ*, 114, 1771  
 Falcón-Barroso J., et al., 2006, *MNRAS*, 369, 529  
 Ferrarese L., 2002, *ApJ*, 578, 90  
 Ferrarese L., Ford H., 2005, *Space Science Reviews*, 116, 523  
 Ferrarese L., Merritt D., 2000, *ApJ*, 539, L9  
 Ferrarese L., Mould J. R., Stetson P. B., Tonry J. L., Blakeslee J. P., Ajhar E. A., 2007, *ApJ*, 654, 186  
 Gebhardt K., 2004, in Ho L. C., ed., *Coevolution of Black Holes and Galaxies The Stellar-Dynamical Search for Supermassive Black Holes in Galactic Nuclei*. pp 1  
 Gebhardt K., et al. 2000, *AJ*, 119, 1157  
 Gebhardt K., et al. 2003, *ApJ*, 583, 92  
 Gebhardt K., et al., 2007, *ApJ*, 671, 1321  
 Gerhard O., Kronawitter A., Saglia R. P., Bender R., 2001, *AJ*, 121, 1936  
 Gerhard O. E., 1993, *MNRAS*, 265, 213  
 Graham A. W., 2008, *PASA*, in press (arXiv:0807.2549)  
 Graham A. W., Erwin P., Caon N., Trujillo I., 2001, *ApJ*, 563, L11  
 Granato G. L., De Zotti G., Silva L., Bressan A., Danese L., 2004, *ApJ*, 600, 580  
 Häring N., Rix H.-W., 2004, *ApJ*, 604, L89

- Häring-Neumayer N., Cappellari M., Rix H.-W., Hartung M., Prieto M. A., Meisenheimer K., Lenzen R., 2006, *ApJ*, 643, 226
- Hoaglin D. C., Mosteller F., Tukey J. W., 1983, *Understanding robust and exploratory data analysis*. Wiley Series in Probability and Mathematical Statistics, New York, 1983, edited by Hoaglin, David C.; Mosteller, Frederick; Tukey, John W.
- Houghton R. C. W., Magorrian J., Sarzi M., Thatte N., Davies R. L., Krajnović D., 2006, *MNRAS*, 367, 2
- Hui X., Ford H. C., Freeman K. C., Dopita M. A., 1995, *ApJ*, 449, 592
- Israel F. P., 1998, *A&A Rev.*, 8, 237
- Jarrett T. H., Chester T., Cutri R., Schneider S. E., Huchra J. P., 2003, *AJ*, 125, 525
- Joseph C. L., et al., 2001, *ApJ*, 550, 668
- Kelson D. D., Illingworth G. D., van Dokkum P. G., Franx M., 2000, *ApJ*, 531, 159
- Kleinmann S. G., Hall D. N. B., 1986, *ApJS*, 62, 501
- Koopmans L. V. E., Treu T., Bolton A. S., Burles S., Moustakas L. A., 2006, *ApJ*, 649, 599
- Kormendy J., 2004, in Ho L. C., ed., *Coevolution of Black Holes and Galaxies The Stellar-Dynamical Search for Supermassive Black Holes in Galactic Nuclei*. pp 1
- Kormendy J., Richstone D., 1995, *ARA&A*, 33, 581
- Krajnović D., et al., 2008, *MNRAS*, 390, 93
- Krajnović D., Cappellari M., de Zeeuw P. T., Copin Y., 2006, *MNRAS*, 366, 787
- Krajnović D., Cappellari M., Emsellem E., McDermid R. M., de Zeeuw P. T., 2005, *MNRAS*, 357, 1113
- Krajnović D., Sharp R., Thatte N., 2007, *MNRAS*, 374, 385
- Kroupa P., 2001, *MNRAS*, 322, 231
- Lauer T. R., et al., 1995, *AJ*, 110, 2622
- Lynden-Bell D., 1969, *Nature*, 223, 690
- Lyubenova M., Kuntschner H., Silva D. R., 2008, *A&A*, 485, 425
- Magorrian J., et al. 1998, *AJ*, 115, 2285
- Malin D. F., Quinn P. J., Graham J. A., 1983, *ApJ*, 272, L5
- Maraston C., 2005, *MNRAS*, 362, 799
- Marconi A., Capetti A., Axon D. J., Koekemoer A., Macchetto D., Schreier E. J., 2001, *ApJ*, 549, 915
- Marconi A., Hunt L. K., 2003, *ApJ*, 589, L21
- Marconi A., Pastorini G., Pacini F., Axon D. J., Capetti A., Macchetto D., Koekemoer A. M., Schreier E. J., 2006, *A&A*, 448, 921
- Marconi A., Schreier E. J., Koekemoer A., Capetti A., Axon D., Macchetto D., Caon N., 2000, *ApJ*, 528, 276
- McLure R. J., Dunlop J. S., 2002, *MNRAS*, 331, 795
- Milosavljević M., Merritt D., 2001, *ApJ*, 563, 34
- Neumayer N., Cappellari M., Reunanen J., Rix H.-W., van der Werf P. P., de Zeeuw P. T., Davies R. I., 2007, *ApJ*, 671, 1329
- Nowak N., Saglia R. P., Thomas J., Bender R., Davies R. I., Gebhardt K., 2008, *MNRAS*, in press (arXiv:0705.1758)
- Nowak N., Saglia R. P., Thomas J., Bender R., Pannella M., Gebhardt K., Davies R. I., 2007, *MNRAS*, 379, 909
- Peng E. W., Ford H. C., Freeman K. C., 2004a, *ApJ*, 602, 705
- Peng E. W., Ford H. C., Freeman K. C., 2004b, *ApJ*, 602, 685
- Pizzella A., Corsini E. M., Dalla Bontà E., Sarzi M., Coccatto L., Bertola F., 2005, *ApJ*, 631, 785
- Quillen A. C., Graham J. R., Frogel J. A., 1993, *ApJ*, 412, 550
- Quinlan G. D., Hernquist L., 1997, *New Astronomy*, 2, 533
- Rejkuba M., 2004, *A&A*, 413, 903
- Richstone D. O., Tremaine S., 1988, *ApJ*, 327, 82
- Riffel R. A., Storchi-Bergmann T., Winge C., McGregor P. J., Beck T., Schmitt H., 2008, *MNRAS*, 385, 1129
- Rix H.-W., de Zeeuw P. T., Cretton N., van der Marel R. P., Carollo C. M., 1997, *ApJ*, 488, 702
- Rusin D., Kochanek C. S., Keeton C. R., 2003, *ApJ*, 595, 29
- Salpeter E. E., 1955, *ApJ*, 121, 161
- Schwarzschild M., 1979, *ApJ*, 232, 236
- Shapiro K. L., Cappellari M., de Zeeuw T., McDermid R. M., Gebhardt K., van den Bosch R. C. E., Statler T. S., 2006, *MNRAS*, 370, 559
- Silge J. D., Gebhardt K., 2003, *AJ*, 125, 2809
- Silge J. D., Gebhardt K., Bergmann M., Richstone D., 2005, *AJ*, 130, 406
- Silk J., Rees M. J., 1998, *A&A*, 331, L1
- Siopis C., et al., 2008, *ApJ*, submitted (arXiv:0808.4001)
- Statler T., 1995, *AJ*, 109, 1371
- Thomas J., Saglia R. P., Bender R., Thomas D., Gebhardt K., Magorrian J., Corsini E. M., Wegner G., 2007, *MNRAS*, 382, 657
- Tonry J. L., Dressler A., Blakeslee J. P., Ajhar E. A., Fletcher A. B., Luppino G. A., Metzger M. R., Moore C. B., 2001, *ApJ*, 546, 681
- Tremaine S., et al. 2002, *ApJ*, 574, 740
- Valluri M., Ferrarese L., Merritt D., Joseph C. L., 2005, *ApJ*, 628, 137
- van de Ven G., de Zeeuw P. T., van den Bosch R. C. E., 2008, *MNRAS*, 385, 614
- van den Bosch R. C. E., van de Ven G., Verolme E. K., Cappellari M., de Zeeuw P. T., 2008, *MNRAS*, 385, 647
- van der Marel R. P., 1994, *MNRAS*, 270, 271
- van der Marel R. P., Cretton N., de Zeeuw P. T., Rix H.-W., 1998, *ApJ*, 493, 613
- van der Marel R. P., Franx M., 1993, *ApJ*, 407, 525
- Verolme E. K., Cappellari M., Copin Y., van der Marel R. P., Bacon R., Bureau M., Davies R. L., Miller B. M., de Zeeuw P. T., 2002, *MNRAS*, 335, 517
- Wallace L., Hinkle K., 1997, *ApJS*, 111, 445
- Wilkinson A., Sharples R. M., Fosbury R. A. E., Wallace P. T., 1986, *MNRAS*, 218, 297